High-Definition Simulation of Packed-Bed Liquid Chromatography

Jayghosh Subodh Rao[a,b,f], Andreas Püttmann[a,b], Siarhei Khirevich[c,e], Ulrich Tallarek[c], Christophe Geuzaine[d], Marek Behr[b,f], Eric von Lieres[a,f]

[a] *Forschungszentrum Jülich, IBG-1: Biotechnology, 52425 Jülich, Germany*
[b] *Chair for Computational Analysis of Technical Systems (CATS), RWTH Aachen University, 52056 Aachen, Germany*
[c] *Department of Chemistry, Philipps-University Marburg, 35032 Marburg, Germany*
[d] *Université de Liège, Department of Electrical Engineering And Computer Science, Montefiore Institute, 4000 Liège, Belgium*
[e] *Current address: Ali I. Al-Naimi Petroleum Engineering Research Center, King Abdullah University of Science and Technology, Thuwal, Saudi Arabia*
[f] *JARA - Center for Simulation and Data Science*

Abstract

Numerical simulations of chromatography are conventionally performed using reduced-order models that homogenize aspects of flow and transport in the radial and angular dimensions. This enables much faster simulations at the expense of lumping the effects of inhomogeneities into a column dispersion coefficient, which requires calibration via empirical correlations or experimental results. We present a high-definition model with spatially resolved geometry. A stabilized space-time finite element method is used to solve the model on massively parallel high-performance computers. We simulate packings with up to $10,000$ particles. The impact of particle size distribution on velocity and concentration profiles as well as breakthrough curves is studied. Our high-definition simulations provide unique insight into the process. The high-definition data can also be used as a source of ground truth to identify and calibrate appropriate reduced-order models that can then be applied for

process design and optimization.

Keywords: packed-bed, chromatography, convection-diffusion-reaction, stabilized space-time finite elements, reduced-order modeling

---

1. Introduction

1.1. Chromatography

Chromatography is an essential separation process used in the biotechnology and pharmaceutical industries as part of downstream processing of liquid solutions. Several types of chromatographic methods use differing principles in order to separate the target components from impurities. They differ in flow geometry (packed-bed, membrane, monolith) and in surface functionalization (ion exchange, hydrophobic interaction, affinity). In packed-bed liquid chromatography, the solution is pumped through a column densely filled with porous particles. Chemical species (components) in the solution are convected along the column through the interstices of the packed-bed, and they diffuse into the porous particles where they are selectively adsorbed to functionalized inner surfaces, e.g., through ion-exchange. This selective adsorption affects the residence times of different components, allowing temporal separation of multiple species at the column outlet. An illustration of the packed-bed chromatographic process is given in Figure 1.

Chromatography columns can be operated in different process schemes, the most simple being flow-through mode. Another commonly applied chromatography process scheme contains three steps: load, wash, and elution. The load phase starts with the input of a mixed solution to the column, and ideally ends with the saturation of all particles. In practice, the parti-

cles towards the column end are only partially loaded due to mass transfer-limitations to avoid loss of target product. The wash phase involves flushing the column with fresh buffer solution that does not contain the components that are to be separated. Finally, the adsorbed molecules are eluted by means of a mobile phase modifier, i.e., a salt in ion-exchange chromatography. The separation is sensitive to the adsorption affinities of the various components with respect to the chemically functionalized interior surfaces of the porous particles. Column geometry, packing structure, particle geometry, and relative concentrations of the components also affect the separation process. Numerical simulations can provide quantitative insights into the process and subsequently help tailor columns and operating conditions for efficient separation of the target molecules.

1.2. Modeling

Chromatography is conventionally modeled using reduced-order models (ROMs) such as the so-called General Rate Model (GRM), Equilibrium Dispersive Model (EDM), and Lumped Kinetic Model (LKM) [1]. The greatest advantage of these models is their simplicity, allowing quick solves and enabling their use in parameter fitting and optimization studies. On the other hand, these models homogenize dispersive effects caused by geometrical features such as particle shape, particle size distribution (PSD) in poly-disperse column packings, and radial porosity variations that are particularly evident in thin columns. Radial and angular flow and dispersion are neglected due to reduction of model dimensions. Moreover, axial velocity and packing porosity have constant averaged values throughout the column. The effects of these homogenizations are lumped into other mechanisms, whose parameters

need to be calibrated using experimental data. In particular, the dispersion coefficient accounts for effects that are caused by small eddies and different flow paths through the packed-bed which are not mechanistically captured by ROMs.

Spatially resolved models of chromatography require more effort and resources in terms of modeling, software development and maintenance, and computational costs, but their results are equally rewarding. These High-Definition (HD) models provide a three-dimensional view into the column, and can be used in conjunction with non-invasive scanning techniques such as MRI [2] and CLSM [3, 4, 5, 6, 7] to reconstruct packings and also analyze flow and mass transport [8, 9, 10, 11, 12, 13, 14, 15] within the column and packed-bed. With developments in 3D printed substrates and monolithic columns, HD simulations provide a distinct advantage over reduced-order simulations, especially when paired with image based reconstruction techniques [2, 16, 17, 5, 6, 7]. Furthermore, these simulations can be used with models of progressively reduced order to isolate and quantify the effect of inhomogeneities that are lumped into axial and radial dispersion coefficients.

In literature, simulations of spatially resolved packed-beds have been conducted primarily with a focus on hydrodynamics. Most simulations focus on thin columns with short packed-beds due to the computational costs associated with scaling the column geometry. Furthermore, many such studies are performed with commercial software such as ANSYS [18, 19, 20], COMSOL [21, 22, 23, 24], and STAR-CCM+ [25, 26, 27, 28, 29], which were at the beginning of this study not ideally suited to massive parallelization.

Several works focus on the effect of column geometry [30, 26, 22], particle

geometry [31, 19] and pore size [20] on pressure drop along the bed. Fairly comprehensive reviews of literature on particle-resolved modeling of fixed-bed reactors are provided by Jurtz et al. [32] and Dixon et al. [33]. While providing a concise overview of models and methods employed, the focus of these reviews is on gas-flow catalytic reactor systems.

Very few papers are dedicated to 3D simulation of chromatography, i.e., flow, transport, and adsorption and desorption in packed-bed columns [21, 34, 22]. Schnittert et al. extended the general rate model to 3D simulations of columns with up to 150 particles using COMSOL. Gerontas et al. also used COMSOL to simulate Langmuir adsorption on a microfluidic column with 4700 particles.

Lattice Boltzmann (LB) simulations are favored in simulating flow in larger columns due to their inherent scalability. Additionally, mesh generation is much simpler due to the Cartesian grid cut-cell approach used. Compared to macroscopic Finite Element (FE) or Finite Volume (FV) methods, the LB method derives averaged macroscopic properties from a particle collision description on a lattice structure. Tallarek et al. use LB to solve flow and transport problems in randomly packed chromatography columns and other porous media [35, 36, 37, 38, 39, 40, 41]. While LB simulations are inherently scalable, the cut-cell meshes used in that method are not suited to cases where the exact effects of the packed-bed morphology are to be studied. However, LB has recently been combined with molecular dynamics for multi-scale simulations of porous media to study diffusion at the mesopore scale [42, 43].

In a previous study, Püttmann et al. present a stabilized Galerkin space-

time FE method to solve the packed-bed chromatography problem [34]. Three benchmark tests were conducted: 1) single component adsorption in 2D, 2) competitive adsorption in 2D, and 3) single component adsorption in 3D. These test cases contained a maximum of 750 mono-disperse particles, i.e., with constant particle size.

1.3. Scope

In the present work, the chromatography process is formulated as a weak coupling between flow and transport-reaction problems: Stokes flow is solved in the interstitial (inter-particle) domain (also referred to as bulk region) and the resulting stationary velocity field is used to model convection of the solution in subsequent mass transfer simulations. In these transport-reaction simulations, convection-diffusion are modeled in the inter-particle domain, and diffusion-reaction (adsorption/desorption) are modeled in the intra-particle domain. The geometry of the inter-particle domain is fully resolved to study its impact on dispersion. The internal pore structure of the particles is homogenized, as in customary reduced order models, to maintain computational tractability. Multi-domain coupling is achieved using diffusive flux continuity at the interface of both these domains. For a detailed mathematical formulation of the governing equations, multi-domain coupling, and boundary conditions, the reader is referred to [44].

Chromatography columns can be characterized using breakthrough experiments. In this mode, the column is continuously loaded with sample molecules until it is fully saturated. This results in a so-called breakthrough curve (BTC) at the column outlet that can be used to assess the axial dispersion in the column. We simulate breakthrough experiments using multi-

domain flow, convection, diffusion, and adsorption for packings with approximately $10,000$ particles in cylindrical columns with ratio of column to particle diameters $\frac{\varnothing_c}{\varnothing_p} \approx 10$. The model and implementation described in [34] are used with modifications to the stabilization parameter. In contrast to previous work, we use here the metric stabilization parameter [45] instead of the 1D GLS stabilization parameter on account of reduced numerical diffusion. For estimating the accuracy of our simulations, we use the generalized holdup volume, which can be calculated both analytically and numerically.

We perform a mesh convergence study on a short column test case with ca. 1000 particles. Large-scale simulations were performed on medium-sized meshes of longer columns with approximately 10 times more particles. Simulations of finer meshes would require extensive modification to the solver and the mesh format. We compare packed-beds with and without PSD and fit the axial dispersion coefficient of the GRM to the results of our HD simulations. The effect of PSD as well as axial and radial position on particle loading are also analyzed.

The goal of this study is to demonstrate the viability of HD models in simulating chromatography processes. These simulations provide insights into complex transport mechanisms within column and particles that are difficult if not impossible to observe experimentally or to simulate with conventional ROM techniques. The resulting HD data allow to calibrate ROMs that can then be utilized for process analysis and design.

2. Model

In this section, we formulate our model assumptions and equations. Figure 2 shows a 2D schematic representation of the HD chromatography column model, which consists of two domains: the inter-particle region Ω_1 and the intra-particle region Ω_2. Due to low solute concentrations, the velocity field calculated in the flow simulation is assumed to be stationary and independent of concentration changes in the transport simulation. Due to low Reynolds numbers ($Re < 1$), a laminar and stationary flow-field is assumed in Ω_1. This allows distinct flow and transport simulations to be solved separately in a weakly coupled manner. Ω_2 is assumed to be devoid of advective flow as extreme pressure would be required to achieve advective flow in the particles due to the small size of the intra-particle pores. Intra-particle flow can be invoked in some macro-porous materials but is not in the scope of this study. In the transport simulations, time-dependent equations are solved in both domains. Convection-diffusion equations are solved in Ω_1 and diffusion-reaction equations are solved in Ω_2. Here, reaction refers to the adsorption and desorption of solute molecules to and from inner particle surfaces, which is described by the Langmuir model. The boundary nodes between the two domains are doubled so as to allow a discontinuity in the solution of the solid phase concentration at the particle surfaces. At this boundary between the bulk and particle domains, we apply a flux continuity constraint.

2.1. Fluid flow

In most liquid chromatography columns, viscous forces dominate over inertial forces. These cases where $Re < 1$ are categorized as 'creeping flow'

and are modeled with the Stokes equations as:

$$\mu \nabla^2 \mathbf{u} + \nabla p = 0 \qquad \text{in } \Omega_1 \tag{1a}$$

$$\nabla \cdot \mathbf{u} = 0 \qquad \text{in } \Omega_1 \tag{1b}$$

where $\mathbf{u}$ is the flow velocity, p is the pressure, and μ is the viscosity. On the boundaries, we have:

$$\mathbf{u} = 0 \qquad \text{on } \Gamma_{wall} \cup \Gamma_{surf} \tag{2a}$$

$$\mathbf{u} = u_z^{in} \qquad \text{on } \Gamma_{in} \tag{2b}$$

$$-p\mathbf{n} + \mu \mathbf{n} \cdot \left(\nabla \mathbf{u} + \nabla \mathbf{u}^T \right) = 0 \qquad \text{on } \Gamma_{out} \tag{2c}$$

where ρ is the density, Γ_{in}, Γ_{out}, Γ_{surf}, and Γ_{wall} are inlet, outlet, particle surface and column wall surfaces, respectively, u_z^{in} is the specified inlet velocity, and $\mathbf{n}$ is the outward normal vector at the column outlet.

2.2. Mass transport

In the multi-domain mass transfer simulations, diffusive flux continuity is used as surface coupling mechanism at the particle surfaces. In the bulk domain (Ω_1) we solve the convection-diffusion problem, and in the particle domain (Ω_2) we solve the coupled diffusion-adsorption equations. In the bulk region, we have:

$$\frac{\partial c_b}{\partial t} + (\mathbf{u} \cdot \nabla) c_b = D_b \nabla^2 c_b \qquad \text{in } \Omega_1 \tag{3}$$

where c_b is the concentration of the solute molecules in the bulk phase, and D_b is the free molecular diffusivity of the solute molecules. In the particle interior (Ω_2), we have:

$$\varepsilon_p \frac{\partial c_p}{\partial t} + (1 - \varepsilon_p) \frac{\partial c_s}{\partial t} = D_p \varepsilon_p \nabla^2 c_p \qquad \text{in } \Omega_2 \quad (4)$$

where c_p is the pore phase concentration, c_s is the solid phase concentration, D_p is the effective pore molecular diffusivity, and ε_p is the particle porosity. Adsorption and desorption is described by the single-component Langmuir model:

$$\frac{\partial c_s}{\partial t} - k_a c_p \left(c_s^{max} - c_s\right) + k_d c_s = 0 \qquad \text{in } \Omega_2 \quad (5)$$

where k_a and k_d are the adsorption and desorption coefficients, and c_s^{max} is the maximum binding capacity.

The bulk concentration c_b is prescribed at the inlet (Γ_{in}). On the other column surfaces ($\Gamma_{out} \cup \Gamma_{wall}$), we have a homogenous Neumann boundary condition. Across particle surfaces (Γ_{surf}), for multi-domain coupling we have a flux continuity condition.

$$c_b = c_{in} \qquad \text{on } \Gamma_{in} \qquad (6a)$$

$$\mathbf{n} \cdot \nabla c_b = 0 \qquad \text{on } \Gamma_{out} \cup \Gamma_{wall} \qquad (6b)$$

$$\mathbf{n_1} \cdot (D_b \nabla c_b) = \mathbf{n_2} \cdot (D_p \varepsilon_p \nabla c_p) \qquad \text{on } \Gamma_{surf} \qquad (6c)$$

The above flux continuity condition automatically ensures $c_b = c_p$ at the domain interface at all times $t > t_0$, provided that the computation is started with $c_b = c_p$ on Γ_{surf} at $t = t_0$.

2.3. Generalized holdup volume

The generalized holdup volume, V_H, of a column is the retention capacity of the column for a given sample. It will be used for measuring the accuracy of our HD simulations. The generalized holdup volume indicates the capacity available for sample molecules within the column. This includes the bulk volume, particle pore volume, and the volume of the sample that is adsorbed in a fully loaded column. While calculating the holdup volume for non-binding scenarios is simple, the generalized holdup volume depends on the binding mechanism and parameters. For the single component Langmuir model, it is possible to analytically calculate the generalized holdup volume as follows:

$$V_H^A = V_b + \varepsilon_p V_p + (1 - \varepsilon_p) V_p \frac{c_s^{max}}{c_b^{in}} \tag{7}$$

where

$$\frac{c_s^{max}}{c_b^{in}} = c_s^{max} \frac{k_a}{k_a c_b^{in} + k_d} \tag{8}$$

Here, V_b is the total volume of the bulk domain and V_p is the total volume of the particle domain.

The generalized holdup volume can also be numerically calculated for any fully developed breakthrough curve, i.e., when the column is fully saturated. The area between the normalized constant inlet concentration and the normalized breakthrough curve, shown in Figure 3, multiplied by the volumetric flow rate, $\dot{V} = \int_A u_z \, dA$, results in the numerical generalized holdup volume of the system:

$$V_H^N = \dot{V} \int_0^\infty (1 - \frac{c_b^{out}}{c_b^{in}})\, dt \tag{9}$$

In our HD simulations, we need to average the concentrations over cross sections A at the column inlet and outlet, respectively. These averages are weighted by the velocity u_z:

$$c^{avg} = \frac{\int_A c u_z dA}{\int_A u_z dA} \tag{10}$$

With that, the numerical holdup volume becomes:

$$V_H^N = \dot{V} \int_0^\infty \left(1 - \frac{\int_A c_b^{out}\ u_z^{out}\ dA}{\int_A c_b^{in}\ u_z^{in}\ dA}\right)\ dt \tag{11}$$

We can now define the ratio of numerical to analytical holdup volumes ϱ:

$$\varrho = \frac{V_H^N}{V_H^A} \tag{12}$$

We also define the relative holdup volume error (ξ) to quantify the error in our simulations:

$$\xi = (\varrho - 1) \times 100\% \tag{13}$$

3. Simulation workflow

Figure 4 shows a flowchart of the general simulation workflow for HD chromatography models. Modeling details and computational tools are described in the following.

3.1. Packing generation

The packed-bed geometry is a central feature of HD chromatography simulations. 3D packings of rigid spheres can be generated computationally [46, 47, 48, 49, 50, 51] or be captured from real packed-beds using high-resolution scanning techniques such as Magnetic Resonance Imaging (MRI), Focused Ion Beam (FIB), Confocal Laser Scanning Microscopy (CLSM), etc. [37, 7, 52, 53]. The particle packing used in our work is generated computationally using a modified Jodrey-Tory algorithm [35, 46]. This algorithm starts with a random distribution of spheres that may overlap within a confinement. In subsequent steps, spheres are iteratively moved and resized to increase packing density while avoiding overlaps. One of the advantages of this method is the ability to generate packings of different porosities. The packings used in this work are cut sections of larger pre-generated packed-beds with $150K$ mono-disperse particles and $15K$ poly-disperse particles.

3.2. Contact points

Point contacts between individual particles, and also between particles and the column wall, pose a challenge in meshing the interstitial region around them. Due to the curvature of the particles, reducing the element size results in higher aspect ratios in the interstitial region, tending towards degeneracy, for elements close to contact points. This issue can be avoided by modifying the contact points in two ways: 1) remove the point contact, and 2) convert it to an area contact. These modifications can be applied either globally to the entire particle, or locally near the contact points [54, 18, 55, 28, 29]. Global modifications either enlarge or reduce all the particles in the packed-bed. Local modifications either add or remove material to/from the contact

region. Figure 5 illustrates the different modifications. While local modifications are shown to provide more accurate pressure fields [54], applying local modifications for large columns can become intractable due to the sheer amount of necessary Boolean operations.

Contact point modifications affect the packed-bed volume and the resulting column porosity, along with the flow profile in the contact region. While local methods such as capping and bridging change the bed volume the least, they are more challenging to generate and computationally harder to scale for larger columns, especially in packings with a high degree of poly-dispersity. In our simulations we hence globally reduce the particle radius by 0.03%, resulting in a 0.09% change in the packed-bed volume. This approach enables fast mesh generation while hardly affecting the packed-bed volume and the local flow field.

An alternative approach could be to consider the softness of the Sepharose beads in the generation of the packed bed, which would naturally result in contact areas. However, such structural mechanics simulations would add complexity beyond the scope of this publication.

3.3. Mesh generation

A chromatography mesh generation tool (genmesh) that uses GMSH [56] and OpenCASCADE was developed for this project. Given the packing data, which consists of particle center coordinates and diameters, genmesh performs the necessary geometric operations and generates the mesh. A typical operation chain roughly consists of the following steps:

1. Extract sections of desired length from larger packing data

2. Add or remove particles to obtain target porosity value
3. Create container and packing geometries
4. Modify contact points
5. Create named physical groups to set boundary conditions
6. Generate mesh

The element size within the particles is uniform throughout the mono-disperse mesh, but scaled by average particle radius in the poly-disperse case. Due to smaller particles having higher curvatures, a uniform element size would not suitably capture the surface of the spherical particles. Magnified images of the mono-disperse and poly-disperse meshes on particle surfaces are shown in Figure 6.

3.4. Mesh partitioning

When the size of the mesh is small enough, it can be solved as a whole on one computer or workstation. The large meshes used in this work, on the other hand, require a cluster of interconnected compute nodes, typically numbering in the thousands. Solving the system in parallel on such a cluster with distributed memory requires that each individual process contains a chunk of the mesh on which the fluid flow and mass transfer problems are solved. Hence the mesh must be partitioned into smaller chunks and distributed among these processes. We use the parallel graph-based partitioning software ParMETIS for this task.

3.5. Solution

The model is implemented in XNS, a multi-physics solver capable of scaling up to thousands of cores. It uses a stabilized discontinuous-in-time space-

time Galerkin Finite Element (FE) method. In order to solve non-linear systems of equations, XNS utilizes a GMRES solver within a Newton-Raphson iteration. The chromatography model equations and other necessary modifications for handling large data were implemented in XNS. All the simulations for this work were performed using XNS on the JURECA supercomputer at Jülich Supercomputing Center (JSC).

The applied FE method for HD simulations of packed-bed liquid chromatography has previously been employed to solve a range of 2D and 3D validation cases with up to 750 particles in the packed-bed, in which the scalability of the numerical method has been analysed [57].

3.6. Postprocessing

Since our large-scale meshes are in the range of hundreds of millions of elements, postprocessing needs to be done in a distributed manner as well. The binary simulation output from XNS is converted into Parallel VTK Unstructured (PVTU) files that contain the solution in a distributed format. The Python scripting interface of ParaView is then used to extract the required information in parallel. Specialized ParaView scripts were created to generate the necessary visualizations and analyses shown in this paper.

4. Case study

In this section we present the column geometries, meshes, and model parameters used in our simulations. Considering the computational resources demanded by HD simulations, we first characterize the sensitivity of the solution to the mesh size using a short column with approximately $1,000$ particles. Further simulations were performed using a longer column with

approximately $10,000$ particles. These simulations provide fundamental insight into the interplay of packing morphology and process performance, even though the column length and width is much smaller than typically found in experimental setups.

4.1. Column geometry

We generated mono-disperse and poly-disperse columns with identical porosities at lengths of $2.01mm$ and $16.00mm$. They are henceforth referred to as short mono-disperse (SM), short poly-disperse (SP), long mono-disperse (LM) and long poly-disperse (LP). The column geometries are shown in Figures 7 and 8. Geometry data for the columns is provided in Table 2. All the simulated columns have a radius of $R = 5.01 \times 10^{-4}m$. At both ends of the mono-disperse packed-beds, the columns consist of void space of length $\approx 0.2\varnothing_c$, where $\varnothing_c$ is the column diameter. The mono-disperse packed-bed consists of particles with diameter $\varnothing_p \approx \frac{\varnothing_c}{10}$. Poly-disperse columns were generated to match the column porosity ε_c to that of the corresponding mono-disperse columns. For the large poly-disperse cases, we removed particles from the ends of the extracted section until the final column porosities closely matched those of the mono-disperse counterparts. The PSD of the poly-disperse packed-bed is shown in Figure 9a. It is representative of a measured PSD of Sepharose [58].

Figure 9b shows the axially-averaged porosity profile over column radius for both packing types. Porosities for both columns at the wall are 1, corresponding to the point contact between the spherical particles and the cylinder walls. The cylinder wall imposes a regularity in the radial positions of the particles. As we move towards the column centre, however, the

packing becomes random. For the poly-disperse column, the porosity profile tends to stabilize towards the column centre. The particle size disparity in poly-disperse packings allows smaller particles to nestle in between the larger ones, filling up space more effectively, resulting in the a more even porosity profile in the packing away from the column walls. In the mono-disperse case, larger oscillations are still present at the column center. In columns with higher column to particle diameter ratios ($\frac{\varnothing_c}{\varnothing_p}$), such oscillations vanish towards the column center for mono-disperse particles as well.

4.2. Meshes

For a mesh sensitivity study, unstructured linear tetrahedral meshes for short columns were generated at 5 different refinements. The mesh size is characterized by the element size per average particle diameter. An element size of 0.10 corresponds to 10 elements per particle diameter. The smaller the element size, the higher the number of elements. Henceforth, specific columns and meshes are referred to using the column name suffixed by the element size, e.g., SP-0.04 refers to the short poly-disperse column with an element size of 0.04.

The mesh size is scaled by the particle size in order to capture the curvature of small and large particles alike. Thus we have the same element size globally in the mono-disperse column, whereas the element size within the particles varies based on particle size in poly-disperse columns. Magnified images of these meshes on the particle surfaces of a poly-disperse packing is shown in Figure 10.

4.3. Model setup and parameters

While XNS is fully able to perform load, wash and elution cycles of chromatography, for the purpose of this work we simulate only the loading stage until full breakthrough is achieved. That is, the inlet concentration is kept constant until the column is fully saturated, and the outlet concentration matches the inlet concentration. For all simulations, the initial concentration is zero everywhere in the column.

The chromatography model parameters used in all our simulations were taken from [59] and are given in Table 3. They reflect the binding behavior of lysozyme on blue Sepharose particles.

5. Results and discussions

The simulations in this paper were performed on the JURECA supercomputer at the Jülich Supercomputing Center (JSC). The SM column simulations at various mesh sizes required between $4,000$ to $46,000$ core-hours. The SP column, similarly, required between $4,400$ to $58,000$ core-hours for its simulations from the coarsest to finest element sizes. In both cases between 720 and 1200 cores were used. Since the Stokes flow simulations are in steady-state, they required only a few minutes, whereas the transient mass transfer simulations consumed the majority of the compute time (between 6 to 48 hours). The LM and LP columns were simulated with element sizes of 0.06, and also required up to two days to terminate with 2400 cores.

5.1. Mesh sensitivity study

Meshes were generated at element sizes ranging from 0.10 to 0.04 for the SM and SP column geometries to study the flow and mass transfer charac-

teristics of the system and examine the stability, accuracy, and consistency of the numerical methods used. Breakthrough simulations were performed for the geometries shown in Figure 7 and the meshes shown in Figure 10.

Rapid partial breakthrough, i.e., an initial concentration jump, is observed in Figure 11a due to the short column length of SM and SP geometries. Thus some solute molecules are convected around the packed-bed directly towards the outlet; they do not diffuse into particles. In longer columns, the higher residence time allows solute molecules sufficient time to diffuse into the particles and adsorb.

FE methods are not locally conservative; they only enforce continuity in a weak sense. In order to measure convergence of the Stokes flow simulation, the averaged flow rates in the column at various cross sections along the column length were calculated. This is shown for SP meshes in Figure 11c. We observe a decrease in the mass flux within the packed-bed region of the column that improves as the mesh is refined. The error drops below 1% for element sizes 0.06 and finer.

Figure 11a shows the breakthrough curves for SP meshes. The results of the finest three meshes are almost indistinguishable, while their generalized holdup error, as measured by the ξ metric (Equation 13), slightly decreases from 8% to 3% as shown Table 4 and in Figure 11b.

5.2. Flow field

Flow in a packed-bed of spherical particles can be complex. Fluid flows in interstitial channels that widen and contract between the particles, forcing it to accelerate and decelerate accordingly. Let $\tilde{u}_z^b = u_z^{in}/\varepsilon_c$ denote the average interstitial z velocity in the packed-bed.

Figure 12 shows the x, y, and z components of the normalized velocity field ($\frac{u_i^b}{\tilde{u}_z^b}$) in the central x-y, and y-z planes of the SM geometry. We observe velocity hotspots distributed over the entire bulk domain. The magnitude of these hotspots for u_x and u_y reaches ca. 4 times of $\tilde{u}_z^b$ while hotspots in u_z reach magnitudes of ca. 10 times. Figure 13 indicates the hotspot regions at progressively higher velocity thresholds, where $u_z > n \cdot \tilde{u}_z^b$, with $n \in [1, 5]$.

Figure 14 shows an analysis of volume fractions occupied at these thresholds for different mesh densities. At lower threshold values, the finer meshes capture substantially more hotspot volume as compared to the coarser meshes. At higher threshold values, these differences disappear.

5.3. Transport and adsorption

The transport in the bulk domain is dominated by convection, whereas within the particle domain it is purely diffusion-driven. The diffusion into a particle depends on the bulk phase concentration in the region around it, which in turn depends upon the local flow field and position and size of the given particle and its neighbours. Figures 15 to 17 show snapshots of the normalized bulk, particle pore and solid phase concentrations in the central y-z plane of the SM column at different times (compare Figure 11a), including zoom boxes of specific regions.

A wall effect is clearly visible in these images, i.e., the concentration front progresses faster along the column wall in comparison to the column center. This can be explained by higher porosity (Figure 9b), i.e., lower particle density at the wall. Consequently, the particles in that region have a lower total capacity and are saturated earlier. An increased average velocity at the column wall (Figure 12c) also contributes to the observed wall effect.

If the bulk concentration around a particle is homogeneous, it will be loaded symmetrically. However, inhomogeneities such as wall effects, channeling, and particle size distribution cause the concentration front to advance unevenly within the packed-bed. Asymmetrical boundary conditions at the particle surfaces lead to asymmetrical loading patterns, as illustrated in Figure 15c. This asymmetry is more pronounced for smaller particles and decreases towards the end of the loading process, because the bulk phase concentration reaches equilibrium with the inlet concentration before the larger particles are fully loaded.

5.4. Particle loading

In contrast to ROMs, our HD simulations allow to monitor the loading of individual particles. This resolution allows us to study the impact of particle size and axial positioning upon the loading process. Figure 18 shows loading profiles of all particles in the SM and SP simulations coloured by axial position in the column and the time required for reaching 90% saturation over axial position. Larger particles reach saturation later than smaller particles simply due to larger volume. The plotting order of the loading curves was randomized to avoid bias caused by overlays in the final plot. Similarly, Figure 19 shows loading profiles of all particles in the SP simulations coloured by particle radius and the time required for reaching 90% saturation over the particle radius.

These figures illustrate the impact of particle size distribution. For the mono-disperse packing, the times for reaching 90% saturation are highly correlated with the axial column position, in particular at the column inlet with increasing bandwidth towards the column outlet. This is mainly caused

by the previously discussed wall effect in these very narrow columns. For the poly-disperse packing, the bandwidth of the correlation is much widened, because smaller particles downstream the column can be loaded at similar times as larger particles further upstream the column. Figure 18d and 19b reveal that the 90% loading time is influenced by particle size influences even more than by axial position.

5.5. Large-scale simulations

The impact of PSD on fully developed breakthrough curves is studied using the long mono-disperse (LM) and poly-disperse (LP) columns shown in Figure 8. Both packings are constructed to have the same bed volume, resulting in identical column porosities, as shown in Table 2.

The sizes of usable meshes in XNS is currently limited due to integer representation. Further improvements would have to be made to the binary mesh storage format so that the number of elements can exceed the current limit of 2,147,483,647. Hence, we simulated the LM and LP columns with an element size of 0.06, which yielded a generalized holdup volume error of 8.65% and 6.65% in the mesh sensitivity study for the mono-disperse and poly-disperse cases respectively. This resulted in meshes with 561M and 583M elements in the LM and LP cases respectively. Results of these simulations are shown in Table 5.

Figure 20 shows the normalized bulk, particle pore, and solid phase concentrations in the LP column at three different times. The observed phenomena and trends are similar to those discussed for the shorter columns but more pronounced along the column length. However, these large-scale simulations also allow to quantify the impact of PSD on the BTC, as shown

in Figure 21.

Note that the HD model explicitly describes the root causes of column dispersion, e.g., different trajectories through the packed-bed, including molecular diffusion. The observed differences in BTC shape and slope are mechanistically predicted. In particular, the mass transfer equation in the bulk domain, equation 3, does not include an explicit dispersion term.

As a dimensionally reduced model, the GRM does not explicitly account for the morphology of the packed-bed. Instead, band broadening effects are lumped together and described by an axial dispersion coefficient D_{ax} in place of the molecular diffusion coefficient D_b in the HD model. To simulate the same system, some parameters of the GRM need to be derived from the HD model. For instance, the column porosity is determined by the void fraction of the packed-bed, while average values need to be used for axial velocity and particle diameter. With that, the dispersion coefficient can be estimated from the HD simulated chromatograms for mono-disperse and poly-disperse packings.

Due to the element size of 0.06, a mass flux defect is expected (Figure 11c). This delays the breakthrough and consequently increases the generalized holdup volume. However, the simulated BTC can be rescaled along the time axis by the inverse holdup volume ratio $1/\varrho$. Figure 22 illustrates that the effect of this scaling on the dispersion coefficient is negligible for values of ϱ close to 1. We encounter ratios of $\varrho = 1.082$ (LM) and $\varrho = 1.064$ (LP).

Figure 21 shows the GRM as fitted to the mono-disperse and poly-disperse HD simulated BTC, neglecting the mass transfer resistance in the diffusion

boundary layer at the particle surfaces. The estimated dispersion coefficients are $D_{ax,mono} = 7.73 \cdot 10^{-7} m^2 \cdot s^{-1}$ and $D_{ax,poly} = 13.84 \cdot 10^{-7} m^2 \cdot s^{-1}$. For both packings, the BTC can be reproduced very well. However, the GRM model cannot predict the BTC unless the dispersion coefficient is known. In practice, this coefficient is determined by fitting the GRM to measured chromatogram data or from empirical correlations. For example, an empirical correlation for D_{ax} is given by Rastegar et al. [60]:

$$D_{ax} = 0.7 D_b + \frac{\varnothing_p u_z^{in}}{0.18 + 0.008 Re^{0.59}} \tag{14}$$

where, $Re = \varnothing_p u_z^{in} \rho / \mu$. This results in $D_{ax,rast} = 1.156 \cdot 10^{-7} m^2 \cdot s^{-1}$. Figure 21 illustrates that the differences in $D_{ax,mono}$, $D_{ax,poly}$ and $D_{ax,rast}$ substantially impact the breakthrough GRM simulated curve.

Our HD simulations, in comparison with GRM fits, allow to study and quantify the impact of packing morphology on column dispersion. In the presented case the PSD, which is neglected by customary chromatography models, causes dispersion to increase by almost 80%. Rasmuson [61] argues that smaller particles in a distribution affect initial breakthrough time since they are faster loaded, while larger particles affect the rate of reaching saturation in the breakthrough curve due to slower loading.

Furthermore, HD simulations allow to compare porosity and velocity profiles of mono-disperse and poly-disperse packings over the column radius, as shown in Figure 23a. These profiles are averaged along the column length and azimuthal angle coordinates. It is evident that the velocity profile follows the porosity profile everywhere except near the wall due to the no-slip boundary condition. Furthermore, a slight phase shift can be observed be-

tween the peaks of each pairing. Figure 23b shows the correlation between both, with R^2 scores of 0.81 for the poly-disperse column and 0.57 for the mono-disperse-column. The worse fit for the latter can be attributed to much stronger oscillations of the porosity profile in the column center.

The porosity and velocity profiles can be used to study external mass transfer and to parameterize more advanced ROMs. The two-dimensional general rate model (2D GRM) still homogenizes the packed-bed but accounts for the radial column coordinate [62]. Similarly, the 1D and 2D GRM can be further extended to account for PSD [63]. Future work will address the configuration and validation of GRM extensions with the open-source process simulator CADET, using the HD simulations presented here as ground truth. For this purpose, HD simulated data with clearly defined structural differences is better suited than measurement data with additional errors and uncertainties.

6. Conclusions

In this work, we applied stabilized space-time finite element simulations to particle-resolved HD models of packed-bed liquid chromatography. Computer generated packings of short ($1,000+$ particles) and long ($10,000+$ particles) beds with and without PSD were used to generate computational meshes with linear tetrahedral elements. The FE simulations comprised of two stages: solving the stationary Stokes flow in the interstitial (bulk) domain, and then solving the transport and adsorption equations in both the bulk and particle domains. Simulations were performed using XNS, a massively parallel multi-physics solver, on the JURECA supercomputer at

Forschungszentrum Jülich.

The workflow for our HD simulations is time and resource intensive. Packing generation, mesh generation, partitioning, preconditioning, solution, and even post-processing in HD simulations all require special treatment and knowledge in comparison to ROMs. In spite of the inherent challenges, HD simulations of chromatography provide us with novel insight into the process by enabling visualization and quantitative analysis of impact of packed-bed geometry on flow, transport, and adsorption in chromatography columns. The rich 3D data generated by these simulations can be used to study the effects of geometric inhomogeneities within the column and serve as ground truth for calibrating ROMs.

Analysis of the flow field reveals hotspots with maximum axial velocity reaching ca. 10 times the average reduced-order velocity ($\tilde{u}_z^b = u_z^{in}/\varepsilon_c$). Lateral velocities ($x$ and y directions) also reached ca. 4 times $\tilde{u}_z^b$. The hotspot regions at various velocity lower thresholds were visualized, and analysis of hotspot volumes shows a significant volume fraction exists up to 5 times $\tilde{u}_z^b$. The dependence of the radial velocity profile on the column's radial porosity profile can be linearly regressed.

Visualizations of mass transfer simulations clearly showed the effects of early breakthrough near the column wall due to the increased porosity (wall effect). Non-concentricity in the loading of particles, which would be neglected by ROMs, is also observed. Particle loading plots for individual particles allow to predict the behavior of the given column at varying lengths and particle size distributions.

Breakthrough curves for long columns with $13,845$ mono-disperse and

9,974 poly-disperse particles were used to fit the axial dispersion coefficient in the dimensionally reduced general rate model. Calibrating the GRM with and without PSD result in differing values of the coefficient of axial dispersion, thus enabling quantification of bed morphology on column dispersion.

The largest simulations performed in this study still use geometries that are two orders of magnitude smaller than commercially available micro columns. HD simulations of such columns are generally possible, provided the required compute quota is available. Much wider columns can be HD simulated by neglecting wall effects and using periodic boundary conditions on the lateral column surfaces.

Large-scale simulations require tremendous amount of developmental and computational resources in order to simulate a single unit operation. Simulation of a complete process pipeline would be infeasible at this scale. While our HD simulations cannot directly be used in process design and optimization, the vast amount of data generated by them can be used to understand and calibrate fundamental parameters of ROMs, including column dispersion and external mass transfer. Calibrated ROMs such as the 1D or 2D GRM with or without PSD can then be used for process design and optimization, which can require thousands or even millions of simulation runs. They also allow studying complex effects of non-linear and competitive adsorption, such as self-sharpening fronts or displacement effects.

7. Acknowledgements

This work was conducted during the Ph.D. studies of Andreas Püttmann and Jayghosh Rao. The authors gratefully acknowledge the funding and

support of the JARA-SSD program. The authors also gratefully acknowledge the computing time granted through JARA on the supercomputer JURECA [64, 65] at Forschungszentrum Jülich.

References

[1] G. Guiochon, A. Felinger, D. G. Shirazi, A. M. Katti, Fundamentals of Preparative and Nonlinear Chromatography, second ed., Elsevier Academic Press, Amsterdam, 2006.

[2] M. Mantle, A. Sederman, L. Gladden, Single- and two-phase flow in fixed-bed reactors: Mri flow visualisation and lattice-boltzmann simulations, Chemical Engineering Science 56 (2001) 523–529. URL: http://dx.doi.org/10.1016/s0009-2509(00)00256-6. doi:10.1016/s0009-2509(00)00256-6.

[3] M. Schröder, E. Von Lieres, J. r. Hubbuch, Direct quantification of intraparticle protein diffusion in chromatographic media, The Journal of Physical Chemistry B 110 (2006) 1429–1436. URL: http://www.ncbi.nlm.nih.gov/pubmed/16471694.

[4] S. Sullivan, F. Sani, M. Johns, L. Gladden, Simulation of packed bed reactors using lattice boltzmann methods, Chemical Engineering Science 60 (2005) 3405–3418. URL: http://dx.doi.org/10.1016/j.ces.2005.01.038. doi:10.1016/j.ces.2005.01.038.

[5] D. Hlushkou, S. Bruns, U. Tallarek, High-performance computing of flow and transport in physically reconstructed silica monoliths, Journal of Chromatography A 1217 (2010) 3674–3682.

URL: http://dx.doi.org/10.1016/j.chroma.2010.04.004. doi:10.1016/j.chroma.2010.04.004.

[6] D. Hlushkou, S. Bruns, A. Seidel-Morgenstern, U. Tallarek, Morphology-transport relationships for silica monoliths: From physical reconstruction to pore-scale simulations, Journal of Separation Science 34 (2011) 2026–2037. URL: http://dx.doi.org/10.1002/jssc.201100158. doi:10.1002/jssc.201100158.

[7] D. Hlushkou, U. Tallarek, Analysis of microstructure–effective diffusivity relationships for the interparticle pore space in physically reconstructed packed beds, Journal of Chromatography A 1581-1582 (2018) 173–179. URL: http://dx.doi.org/10.1016/j.chroma.2018.11.003. doi:10.1016/j.chroma.2018.11.003.

[8] A. Ljunglöf, R. Hjorth, Confocal microscopy as a tool for studying protein adsorption to chromatographic matrices, Journal of Chromatography A 743 (1996) 75–83. URL: http://dx.doi.org/10.1016/0021-9673(96)00290-7. doi:10.1016/0021-9673(96)00290-7.

[9] A. Ljunglöf, J. Thömmes, Visualising intraparticle protein transport in porous adsorbents by confocal microscopy, Journal of Chromatography A 813 (1998) 387–395. URL: http://dx.doi.org/10.1016/s0021-9673(98)00378-1. doi:10.1016/s0021-9673(98)00378-1.

[10] J. Hubbuch, T. Linden, E. Knieps, J. Thömmes, M.-R. Kula, Dynamics of protein uptake within the adsorbent particle during packed bed chromatography, Biotechnology and Bioengineering

677 80 (2002) 359–368. URL: http://dx.doi.org/10.1002/bit.10500.
678 doi:10.1002/bit.10500.

679 [11] S. R. Dziennik, E. B. Belcher, G. A. Barker, M. J. DeBergalis, S. E.
680 Fernandez, A. M. Lenhoff, Nondiffusive mechanisms enhance protein
681 uptake rates in ion exchange particles, Proceedings of the National
682 Academy of Sciences 100 (2003) 420–425. URL: http://dx.doi.org/
683 10.1073/pnas.0237084100. doi:10.1073/pnas.0237084100.

684 [12] J. Hubbuch, T. Linden, E. Knieps, J. Thömmes, M.-R. Kula, Mechanism
685 and kinetics of protein transport in chromatographic media studied by
686 confocal laser scanning microscopy, Journal of Chromatography A 1021
687 (2003) 105–115. URL: http://dx.doi.org/10.1016/j.chroma.2003.
688 08.092. doi:10.1016/j.chroma.2003.08.092.

689 [13] K. Yang, Q.-H. Shi, Y. Sun, Modeling and simulation of pro-
690 tein uptake in cation exchanger visualized by confocal laser scan-
691 ning microscopy, Journal of Chromatography A 1136 (2006) 19–28.
692 URL: http://dx.doi.org/10.1016/j.chroma.2006.09.036. doi:10.
693 1016/j.chroma.2006.09.036.

694 [14] K. Yang, S. Bai, Y. Sun, Protein adsorption dynamics in cation-
695 exchange chromatography quantitatively studied by confocal laser
696 scanning microscopy, Chemical Engineering Science 63 (2008)
697 4045–4054. URL: http://dx.doi.org/10.1016/j.ces.2008.05.013.
698 doi:10.1016/j.ces.2008.05.013.

699 [15] G. Zhao, L. Zhang, S. Bai, Y. Sun, Analysis of hydrophobic charge

induction displacement chromatography by visualization with confocal laser scanning microscopy, Separation and Purification Technology 82 (2011) 138–147. URL: http://dx.doi.org/10.1016/j.seppur.2011.09.002. doi:10.1016/j.seppur.2011.09.002.

[16] A. Sederman, P. Alexander, L. Gladden, Structure of packed beds probed by magnetic resonance imaging, Powder Technology 117 (2001) 255–269. URL: http://dx.doi.org/10.1016/s0032-5910(00)00374-0. doi:10.1016/s0032-5910(00)00374-0.

[17] M. Baker, P. Young, G. Tabor, Image based meshing of packed beds of cylinders at low aspect ratios using 3d mri coupled with computational fluid dynamics, Computers & Chemical Engineering 35 (2011) 1969–1977. URL: http://dx.doi.org/10.1016/j.compchemeng.2011.03.017. doi:10.1016/j.compchemeng.2011.03.017.

[18] S. Bu, J. Yang, M. Zhou, S. Li, Q. Wang, Z. Guo, On contact point modifications for forced convective heat transfer analysis in a structured packed bed of spheres, Nuclear Engineering and Design 270 (2014) 21–33. URL: http://dx.doi.org/10.1016/j.nucengdes.2014.01.001. doi:10.1016/j.nucengdes.2014.01.001.

[19] G. M. Karthik, V. V. Buwa, Effect of particle shape on fluid flow and heat transfer for methane steam reforming reactions in a packed bed, AIChE Journal 63 (2016) 366–377. URL: http://dx.doi.org/10.1002/aic.15542. doi:10.1002/aic.15542.

[20] D. Pashchenko, I. Karpilov, R. Mustafin, Numerical calculation with experimental validation of pressure drop in a fixed-bed reactor filled with the porous elements, AIChE Journal 66 (2020). URL: http://dx.doi.org/10.1002/aic.16937. doi:10.1002/aic.16937.

[21] S. Schnittert, R. Winz, E. von Lieres, Development of a 3d model for packed bed liquid chromatography in micro-columns, 2009 Third UKSim European Symposium on Computer Modeling and Simulation (2009). URL: http://dx.doi.org/10.1109/ems.2009.62. doi:10.1109/ems.2009.62.

[22] S. Gerontas, M. S. Shapiro, D. G. Bracewell, Chromatography modelling to describe protein adsorption at bead level, Journal of Chromatography A 1284 (2013) 44–52. URL: http://dx.doi.org/10.1016/j.chroma.2013.01.102. doi:10.1016/j.chroma.2013.01.102.

[23] L. Li, X. Yan, J. Yang, Q. Wang, Computational study of chromatography performance in ordered packed beds with spherical or ellipsoidal particles, Energy Procedia 75 (2015) 3322–3327. URL: http://dx.doi.org/10.1016/j.egypro.2015.07.719. doi:10.1016/j.egypro.2015.07.719.

[24] L. Li, X. Yan, J. Yang, Q. Wang, Numerical investigation on band-broadening characteristics of an ordered packed bed with novel particles, Applied Energy 185 (2017) 2168–2180. URL: http://dx.doi.org/10.1016/j.apenergy.2016.03.045. doi:10.1016/j.apenergy.2016.03.045.

[25] T. Eppinger, K. Seidler, M. Kraume, Dem-cfd simulations of fixed bed reactors with small tube to particle diameter ratios, Chemical Engineering Journal 166 (2011) 324–331. URL: http://dx.doi.org/10.1016/j.cej.2010.10.053. doi:10.1016/j.cej.2010.10.053.

[26] N. Zobel, T. Eppinger, F. Behrendt, M. Kraume, Influence of the wall structure on the void fraction distribution in packed beds, Chemical Engineering Science 71 (2012) 212–219. URL: http://dx.doi.org/10.1016/j.ces.2011.12.029. doi:10.1016/j.ces.2011.12.029.

[27] G. D. Wehinger, T. Eppinger, M. Kraume, Detailed numerical simulations of catalytic fixed-bed reactors: Heterogeneous dry reforming of methane, Chemical Engineering Science 122 (2015) 197–209. URL: http://dx.doi.org/10.1016/j.ces.2014.09.007. doi:10.1016/j.ces.2014.09.007.

[28] G. D. Wehinger, C. Fütterer, M. Kraume, Contact modifications for cfd simulations of fixed-bed reactors: Cylindrical particles, Industrial & Engineering Chemistry Research 56 (2016) 87–99. URL: http://dx.doi.org/10.1021/acs.iecr.6b03596. doi:10.1021/acs.iecr.6b03596.

[29] T. Eppinger, G. D. Wehinger, A generalized contact modification for fixed-bed reactor cfd simulations, Chemie Ingenieur Technik (2020). URL: http://dx.doi.org/10.1002/cite.202000182. doi:10.1002/cite.202000182.

[30] S. Khirevich, A. Höltzel, D. Hlushkou, U. Tallarek, Impact of conduit geometry and bed porosity on flow and dispersion in noncylindri-

769 cal sphere packings, Analytical Chemistry 79 (2007) 9340–9349. URL:
770 http://dx.doi.org/10.1021/ac071428k. doi:10.1021/ac071428k.

771 [31] F. Dorai, C. Moura Teixeira, M. Rolland, E. Climent, M. Marcoux,
772 A. Wachs, Fully resolved simulations of the flow through a packed bed
773 of cylinders: Effect of size distribution, Chemical Engineering Science
774 129 (2015) 180–192. URL: http://dx.doi.org/10.1016/j.ces.2015.
775 01.070. doi:10.1016/j.ces.2015.01.070.

776 [32] N. Jurtz, M. Kraume, G. D. Wehinger, Advances in fixed-bed reac-
777 tor modeling using particle-resolved computational fluid dynamics (cfd),
778 Reviews in Chemical Engineering 35 (2019) 139–190. URL: http://dx.
779 doi.org/10.1515/revce-2017-0059. doi:10.1515/revce-2017-0059.

780 [33] A. G. Dixon, M. Nijemeisland, E. H. Stitt, Packed tubular re-
781 actor modeling and catalyst design using computational fluid dy-
782 namics, Advances in Chemical Engineering (2006) 307–389. URL:
783 http://dx.doi.org/10.1016/s0065-2377(06)31005-8. doi:10.1016/
784 s0065-2377(06)31005-8.

785 [34] A. Püttmann, M. Nicolai, M. Behr, E. von Lieres, Stabilized space–time
786 finite elements for high-definition simulation of packed bed chromatog-
787 raphy, Finite Elements in Analysis and Design 86 (2014) 1–11. doi:10.
788 1016/j.finel.2014.03.001.

789 [35] S. Khirevich, A. Höltzel, D. Hlushkou, U. Tallarek, Impact of con-
790 duit geometry and bed porosity on flow and dispersion in noncylin-

drical sphere packings., Analytical chemistry 79 (2007) 9340–9349. doi:10.1021/ac071428k.

[36] S. Khirevich, A. Höltzel, D. Hlushkou, A. Seidel-Morgenstern, U. Tallarek, Structure-transport analysis for particulate packings in trapezoidal microchip separation channels, Lab on a Chip 8 (2008) 1801–1808. URL: http://dx.doi.org/10.1039/b810688f.

[37] S. Khirevich, A. Höltzel, S. Ehlert, A. Seidel-Morgenstern, U. Tallarek, Large-scale simulation of flow and transport in reconstructed HPLC-microchip packings, Analytical Chemistry 81 (2009) 4937–4945. URL: http://www.ncbi.nlm.nih.gov/pubmed/19459621.

[38] S. Khirevich, A. Daneyko, A. Höltzel, A. Seidel-Morgenstern, U. Tallarek, Statistical analysis of packed beds, the origin of short-range disorder, and its impact on eddy dispersion., Journal of Chromatography A 1217 (2010) 4713–22. URL: http://www.ncbi.nlm.nih.gov/pubmed/20570271. doi:10.1016/j.chroma.2010.05.019.

[39] S. Khirevich, High-Performance Computing of Flow, Diffusion, and Hydrodynamic Dispersion in Random Sphere Packings, Phd thesis, Philipps-Universität Marburg, 2011.

[40] A. Daneyko, S. Khirevich, A. Höltzel, A. Seidel-Morgenstern, U. Tallarek, From random sphere packings to regular pillar arrays: Effect of the macroscopic confinement on hydrodynamic dispersion, Journal of Chromatography A 1218 (2011) 8231–8248. URL: http://www.ncbi.nlm.nih.gov/pubmed/21982445. doi:10.1016/j.chroma.2011.09.039.

[41] A. Daneyko, D. Hlushkou, S. Khirevich, U. Tallarek, From random sphere packings to regular pillar arrays: Analysis of transverse dispersion, Journal of Chromatography A 1257 (2012) 98–115. URL: http://www.ncbi.nlm.nih.gov/pubmed/22921359. doi:10.1016/j.chroma.2012.08.024.

[42] U. Tallarek, D. Hlushkou, J. Rybka, A. Höltzel, Multiscale simulation of diffusion in porous media: From interfacial dynamics to hierarchical porosity, The Journal of Physical Chemistry C 123 (2019) 15099–15112. URL: http://dx.doi.org/10.1021/acs.jpcc.9b03250. doi:10.1021/acs.jpcc.9b03250.

[43] U. Tallarek, D. Hlushkou, A. Höltzel, Solute sorption, diffusion, and advection in macro–mesoporous materials: Toward a realistic bottom-up simulation strategy, The Journal of Physical Chemistry C 126 (2022) 2336–2348. URL: http://dx.doi.org/10.1021/acs.jpcc.1c10137. doi:10.1021/acs.jpcc.1c10137.

[44] A. Püttmann, S. Schnittert, U. Naumann, E. von Lieres, Fast and Accurate Parameter Sensitivities for the General Rate Model of Column Liquid Chromatography, Computers & Chemical Engineering 56 (2013) 46–57. URL: http://linkinghub.elsevier.com/retrieve/pii/S0098135413001440. doi:10.1016/j.compchemeng.2013.04.021.

[45] L. Pauli, M. Behr, On stabilized space-time fem for anisotropic meshes: Incompressible navier-stokes equations and applications to blood flow in medical devices, International Journal for Numerical Methods in Flu-

ids 85 (2017) 189–209. URL: http://dx.doi.org/10.1002/fld.4378. doi:10.1002/fld.4378.

[46] W. S. Jodrey, E. M. Tory, Computer simulation of close random packing of equal spheres, Physical Review A 32 (1985) 2347–2351. URL: http://dx.doi.org/10.1103/physreva.32.2347. doi:10.1103/physreva.32.2347.

[47] B. D. Lubachevsky, F. H. Stillinger, Geometric properties of random disk packings, Journal of Statistical Physics 60 (1990) 561–583. URL: http://dx.doi.org/10.1007/bf01025983. doi:10.1007/bf01025983.

[48] J. Mościński, M. Bargieł, Z. A. Rycerz, P. W. M. Jacobs, The force-biased algorithm for the irregular close packing of equal hard spheres, Molecular Simulation 3 (1989) 201–212. URL: http://dx.doi.org/10.1080/08927028908031373. doi:10.1080/08927028908031373.

[49] G. A. Georgalli, M. A. Reuter, A particle packing algorithm for packed beds with size distribution, Granular Matter 10 (2008) 257–262. URL: http://dx.doi.org/10.1007/s10035-008-0097-z. doi:10.1007/s10035-008-0097-z.

[50] J.-F. Jerier, D. Imbault, F.-V. Donze, P. Doremus, A geometric algorithm based on tetrahedral meshes to generate a dense polydisperse sphere packing, Granular Matter 11 (2008) 43–52. URL: http://dx.doi.org/10.1007/s10035-008-0116-0. doi:10.1007/s10035-008-0116-0.

[51] E. M. B. Campello, K. R. Cassares, Rapid generation of particle packs at high packing ratios for dem simulations of granular compacts, Latin American Journal of Solids and Structures 13 (2016) 23–50. URL: http://dx.doi.org/10.1590/1679-78251694. doi:10.1590/1679-78251694.

[52] C. Jungreuthmayer, P. Steppert, G. Sekot, A. Zankel, H. Reingruber, J. Zanghellini, A. Jungbauer, The 3d pore structure and fluid dynamics simulation of macroporous monoliths: High permeability due to alternating channel width, Journal of Chromatography A 1425 (2015) 141–149. URL: http://dx.doi.org/10.1016/j.chroma.2015.11.026. doi:10.1016/j.chroma.2015.11.026.

[53] A. Martinez, M. Kuhn, H. Briesen, D. Hekmat, Enhancing the x-ray contrast of polymeric biochromatography particles for three-dimensional imaging, Journal of Chromatography A 1590 (2019) 65–72. URL: http://dx.doi.org/10.1016/j.chroma.2018.12.065. doi:10.1016/j.chroma.2018.12.065.

[54] A. G. Dixon, M. Nijemeisland, E. H. Stitt, Systematic mesh development for 3d cfd simulation of fixed beds: Contact points study, Computers & Chemical Engineering 48 (2013) 135–153. URL: http://dx.doi.org/10.1016/j.compchemeng.2012.08.011. doi:10.1016/j.compchemeng.2012.08.011.

[55] S. Rebughini, A. Cuoci, M. Maestri, Handling contact points in reactive cfd simulations of heterogeneous catalytic fixed bed reactors, Chemical

Engineering Science 141 (2016) 240–249. URL: http://dx.doi.org/10.1016/j.ces.2015.11.013. doi:10.1016/j.ces.2015.11.013.

[56] C. Geuzaine, J.-F. Remacle, Gmsh : a three-dimensional finite element mesh generator with built-in pre- and post-processing facilities, International Journal for Numerical Methods in Engineering 0 (2009) 1–24.

[57] A. Püttmann, M. Nicolai, M. Behr, E. von Lieres, Stabilized space–time finite elements for high-definition simulation of packed bed chromatography, Finite Elements in Analysis and Design 86 (2014) 1–11. URL: http://dx.doi.org/10.1016/j.finel.2014.03.001. doi:10.1016/j.finel.2014.03.001.

[58] G. Carta, A. Ubiera, Particle-size distribution effects in batch adsorption, AIChE Journal 49 (2003) 3066–3073. URL: http://dx.doi.org/10.1002/aic.690491208. doi:10.1002/aic.690491208.

[59] R. Montesinos, A. Tejedamansir, R. Guzman, J. Ortega, W. Schiesser, Analysis and simulation of frontal affinity chromatography of proteins, Separation and Purification Technology 42 (2005) 75–84. URL: http://linkinghub.elsevier.com/retrieve/pii/S1383586604001674. doi:10.1016/j.seppur.2004.03.014.

[60] S. O. Rastegar, T. Gu, Empirical correlations for axial dispersion coefficient and peclet number in fixed-bed columns, Journal of Chromatography A 1490 (2017) 133–137. URL: http://dx.doi.org/10.1016/j.chroma.2017.02.026. doi:10.1016/j.chroma.2017.02.026.

[61] A. Rasmuson, The effect of particles of variable size, shape and properties on the dynamics of fixed beds, Chemical Engineering Science 40 (1985) 621–629. URL: http://dx.doi.org/10.1016/0009-2509(85)80006-3. doi:10.1016/0009-2509(85)80006-3.

[62] S. Qamar, D. U. Uche, F. U. Khan, A. Seidel-Morgenstern, Analysis of linear two-dimensional general rate model for chromatographic columns of cylindrical geometry, Journal of Chromatography A 1496 (2017) 92–104. doi:10.1016/j.chroma.2017.03.048.

[63] G. Carta, A. Ubiera, Particle-size distribution effects in batch adsorption, AIChE Journal 49 (2003) 3066–3073. doi:10.1002/aic.690491208.

[64] Jülich Supercomputing Centre, JURECA: Modular supercomputer at Jülich Supercomputing Centre, Journal of large-scale research facilities 4 (2018). URL: http://dx.doi.org/10.17815/jlsrf-4-121-1. doi:10.17815/jlsrf-4-121-1.

[65] Jülich Supercomputing Centre, JURECA: Data Centric and Booster Modules implementing the Modular Supercomputing Architecture at Jülich Supercomputing Centre, Journal of large-scale research facilities 7 (2021). URL: http://dx.doi.org/10.17815/jlsrf-7-182. doi:10.17815/jlsrf-7-182.

Table 1: Nomenclature

Symbol	Meaning	Units
Ω_1	bulk (interstitial) domain	-
Ω_2	particle domain	-
Γ_{in}	column inlet surface	-
Γ_{out}	column outlet surface	-
Γ_{wall}	column wall surface	-
Γ_{surf}	packed-bed surfaces	-
k_a	Adsorption coefficient	$m^3 \cdot mol^{-1} \cdot s^{-1}$
k_d	Desorption coefficient	s^{-1}
c_s^{max}	maximum binding capcity	$mol \cdot m^{-3}$
c_b	bulk phase concentration in Ω_1	$mol \cdot m^{-3}$
c_p	pore phase concentration in Ω_2	$mol \cdot m^{-3}$
c_s	solid phase concentration in Ω_2	$mol \cdot m^{-3}$
c_b^{in}	bulk phase concentration on Γ_{in}	$mol \cdot m^{-3}$
c_b^{out}	bulk phase concentration on Γ_{out}	$mol \cdot m^{-3}$
V_b	bulk domain volume	m^3
V_p	particle domain volume	m^3
D_b	bulk phase diffusivity	$m^2 \cdot s^{-1}$
D_p	effective pore phase diffusivity	$m^2 \cdot s^{-1}$
ε_c	column porosity	$-$
ε_p	particle porosity	$-$
$\mathbf{u}$	velocity	$m \cdot s^{-1}$
u_z^{in}	inlet velocity on Γ_{in}	$m \cdot s^{-1}$

$\tilde{u}_z^b$	averaged interstitial z-velocity	$m \cdot s^{-1}$
μ	dynamic viscosity	$N \cdot s \cdot m^{-2}$
ρ	density	$kg \cdot m^{-3}$
p	pressure	$N \cdot m^{-2}$
$\varnothing_p$	particle diameter	m
$\varnothing_c$	column diameter	m
t_s^{90}	time for 90% particle saturation	s
V_H^A	analytical holdup volume	m^3
V_H^N	numerical holdup volume	m^3
ϱ	holdup volume ratio	$-$
A	cross section area of column	m^2
$\dot{V}$	volumetric flowrate	$m^3 \cdot s^{-1}$
ξ	relative holdup volume error	%

Table 2: Geometrical properties of simulated packed-bed columns.

Identifier	Particle Size Distribution	Column Length (mm)	Number of Particles ($-$)	Avg. Particle Radius (μm)	Column Porosity ($-$)	Bed Porosity ($-$)	Bed Length (mm)
SM	mono-disperse	2.01	1,360	49.99	0.55	0.44	1.61
SP	poly-disperse	2.01	1,002	52.80	0.54	0.44	1.65
LM	mono-disperse	16.00	13,845	49.99	0.43	0.41	16.00
LP	poly-disperse	16.00	9,874	53.14	0.43	0.40	15.36

Table 3: Chromatography model parameters.

Parameter	**Value**	**Unit**
D_b	$1.15 \cdot 10^{-10}$	$m^2 \cdot s^{-1}$
D_p	$7.07 \cdot 10^{-11}$	$m^2 \cdot s^{-1}$
ε_p	0.75	$-$
k_a	1.144	$m^3 \cdot mol^{-1} \cdot s^{-1}$
k_d	$2 \cdot 10^{-3}$	s^{-1}
c_s^{max}	4.88	$mol \cdot m^{-3}$
c_b^{in}	$7.14 \cdot 10^{-3}$	$mol \cdot m^{-3}$
u_z^{in}	$2.09 \cdot 10^{-4}$	$m \cdot s^{-1}$

Table 4: Mesh sensitivity results for SM and SP columns.

Geometry/ Element Size	Elements Interstitial	Elements Total	ξ
SM–0.04	131.34M	244.67M	3.26%
SM–0.05	67.01M	131.86M	5.50%
SM–0.06	39.76M	070.98M	8.65%
SM–0.08	16.86M	031.37M	19.83%
SM–0.10	8.94M	016.74M	41.46%
SP–0.04	143.09M	271.65M	2.67%
SP–0.05	72.30M	142.01M	4.30%
SP–0.06	42.52M	082.57M	6.65%
SP–0.08	18.16M	034.46M	14.28%
SP–0.10	9.57M	018.46M	27.40%

Table 5: Mesh characteristics for LM and LP columns.

Geometry/ Element Size	Elements Interstitial	Elements Total	ξ
LM–0.06	235.88M	561.53M	8.20%
LP–0.06	237.89M	583.79M	6.43%

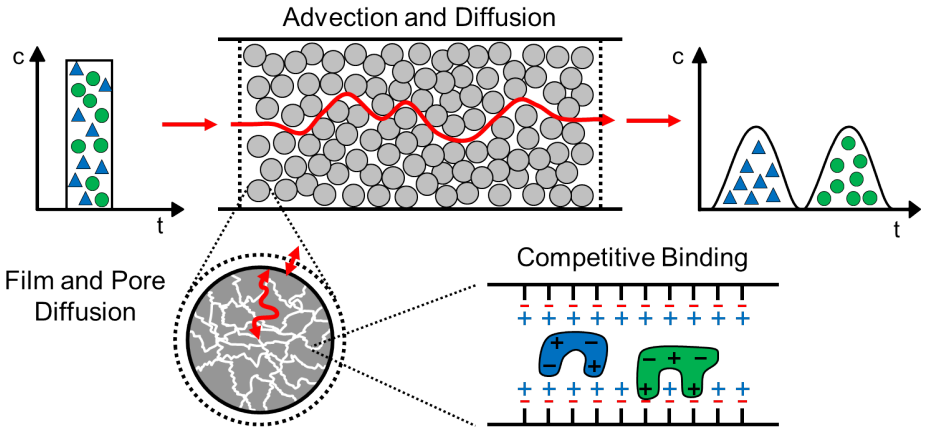

Figure 1: Representation of a chromatography process showing involved mechanisms. Advection and diffusion dominate in the interstices, while diffusion and adsorption dominate within the porous particles.

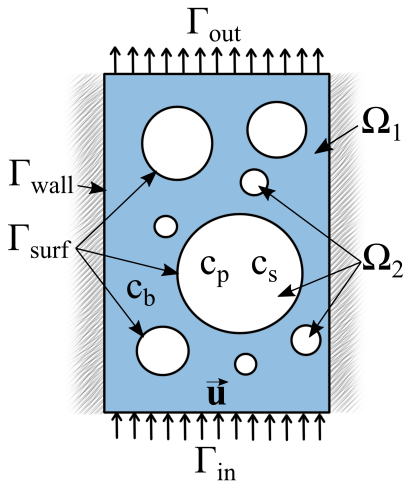

Figure 2: Schematic of domains and domain boundaries of HD chromatography model.

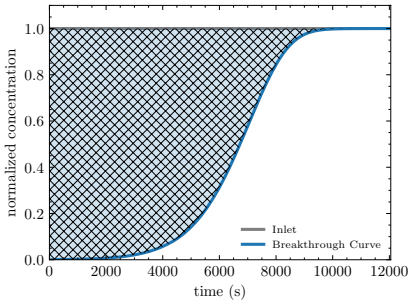

Figure 3: Generalized holdup volume as area over normalized chromatogram.

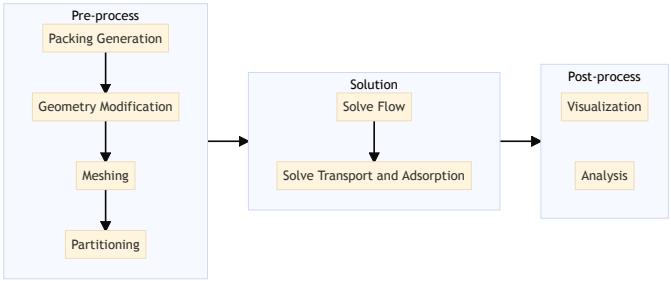

Figure 4: Flowchart of general simulation workflow.

(a) reduced

(b) enlarged

(c) capped

(d) bridged

Figure 5: Contact point modifications illustrated using two particles.

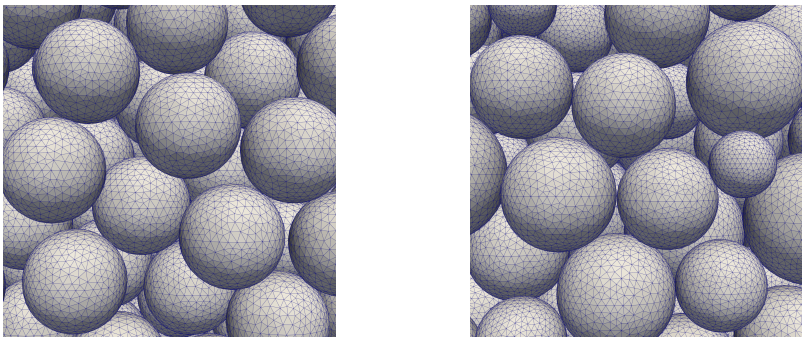

(a) mono-disperse (b) poly-disperse

Figure 6: Magnified meshes of mono-disperse and poly-disperse packings.

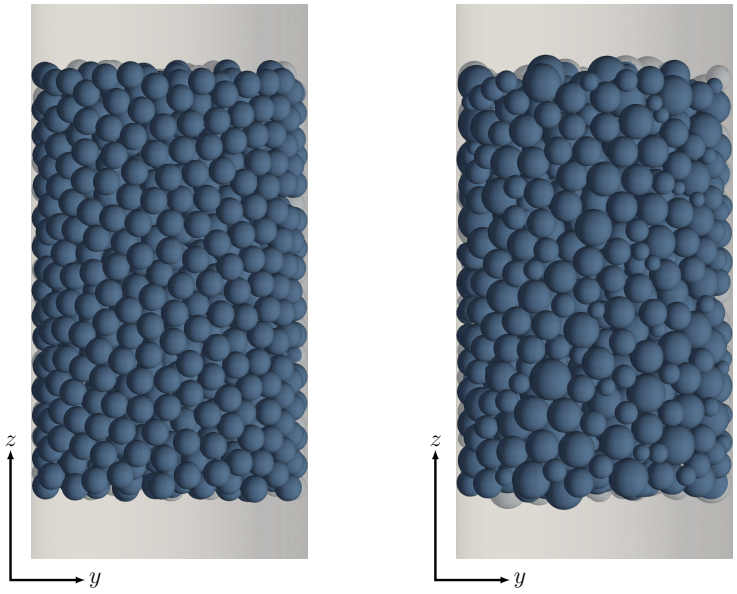

(a) SM packing (b) SP packing

Figure 7: Geometry of short mono-disperse (SM) and short poly-disperse (SP) packings.

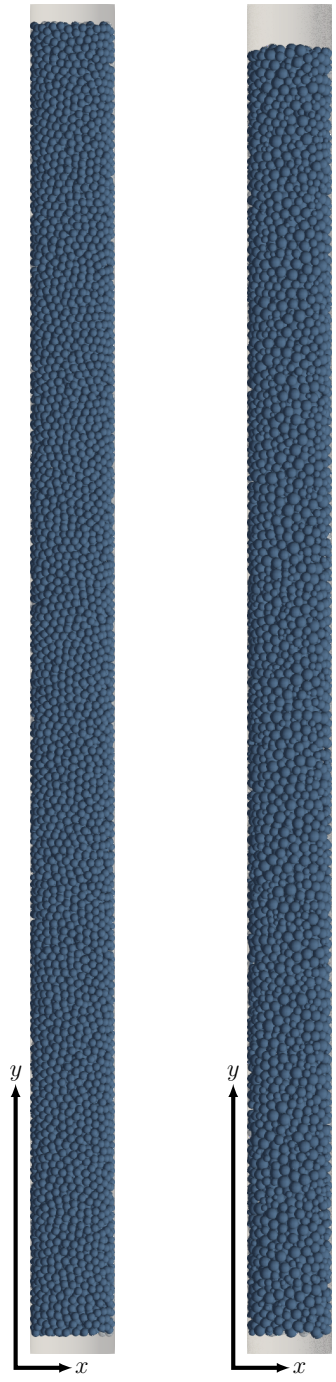

(a) LM packing (b) LP packing

Figure 8: Geometry of long mono-disperse (LM) and long poly-disperse (LP) packings.

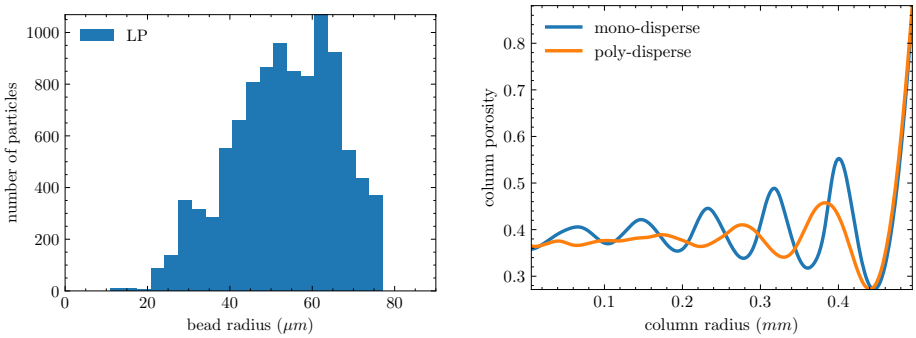

(a) Particle size distribution (b) Porosity profile

Figure 9: PSD of LP packing and porosity profiles of LM and LP packings.

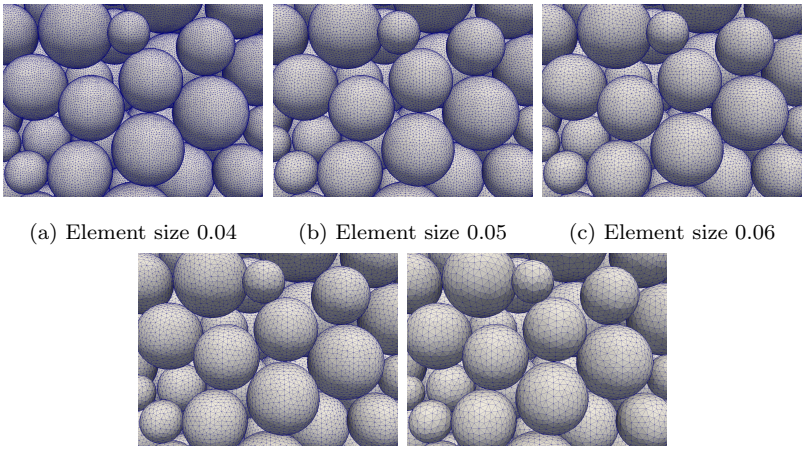

(a) Element size 0.04 (b) Element size 0.05 (c) Element size 0.06

(d) Element size 0.08 (e) Element size 0.10

Figure 10: Zoomed in tetrahedral meshes of poly-disperse packing used for mesh sensitivity study.

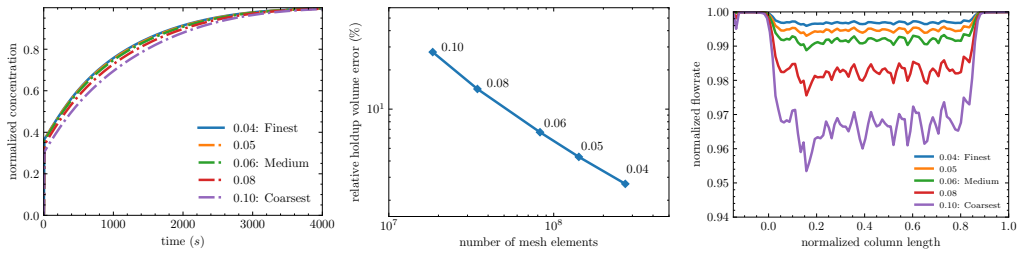

(a) Breakthrough chromatograms (b) Mesh convergence (c) Mass flux error

Figure 11: Results of flow and transport simulations for short poly-disperse column with varying element sizes.

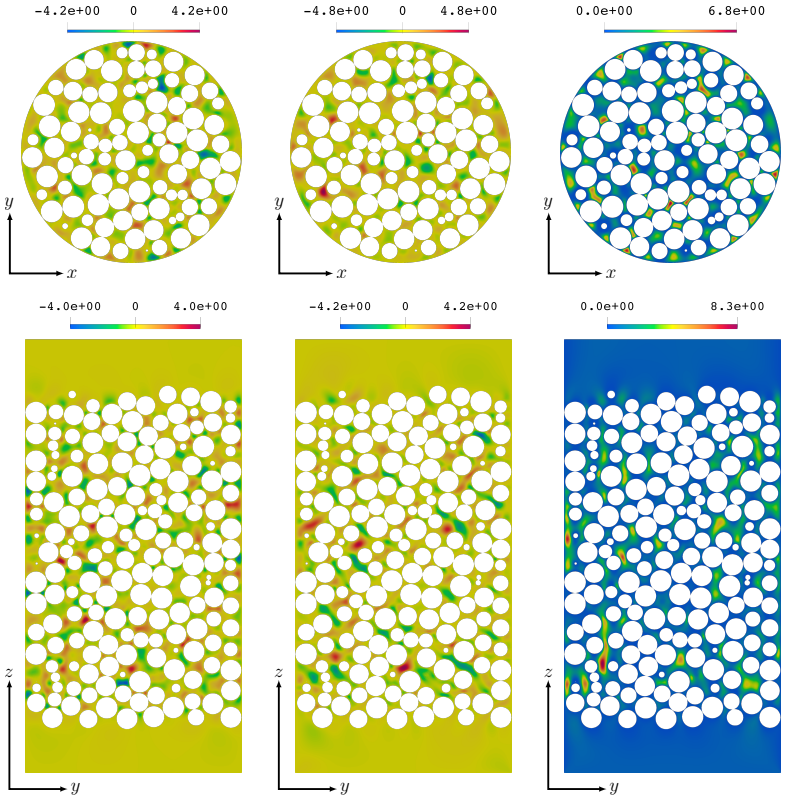

(a) u_x (b) u_y (c) u_z

Figure 12: Normalized velocity components $\frac{u_i^b}{\bar{u}_z^b}$ in central x-y and y-z planes of SM geometry. Direction of flow is upward.

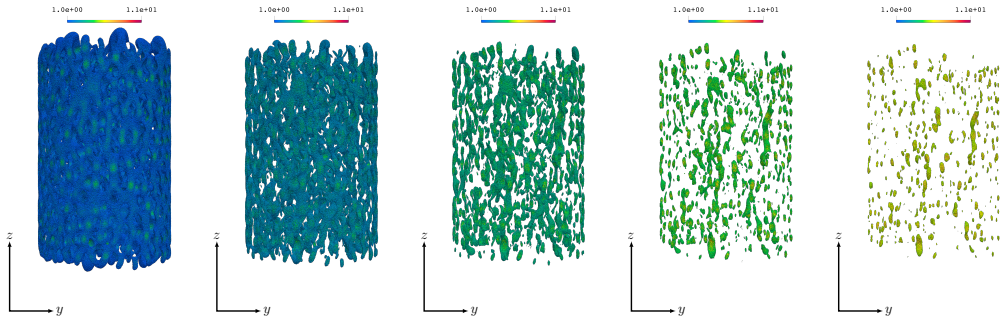

(a) $u_z \geq \tilde{u}_z^b$ (b) $u_z \geq 2\tilde{u}_z^b$ (c) $u_z \geq 3\tilde{u}_z^b$ (d) $u_z \geq 4\tilde{u}_z^b$ (e) $u_z \geq 5\tilde{u}_z^b$

Figure 13: Normalized axial velocity ($\frac{u_z^b}{\tilde{u}_z^b}$) hotspots at various thresholds in SM geometry.

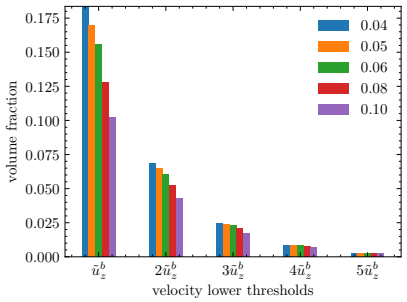

Figure 14: Hotspot volume fraction over velocity threshold for SM geometry.

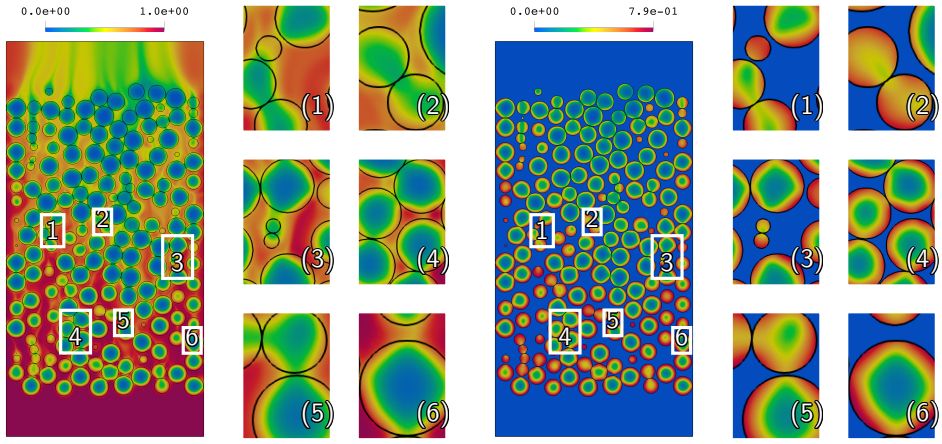

(a) c_b and c_p (b) zoom boxes from (a) (c) c_s (d) zoom boxes from (c)

Figure 15: Normalized bulk ($\frac{c_b}{c_b^{in}}$), particle pore ($\frac{c_p}{c_b^{in}}$) and solid ($\frac{c_s}{c_s^{max}}$) phase concentrations in central y-z plane of SM column at time $t \approx 550s$ with zoom boxes of specific regions. Direction of flow is upward.

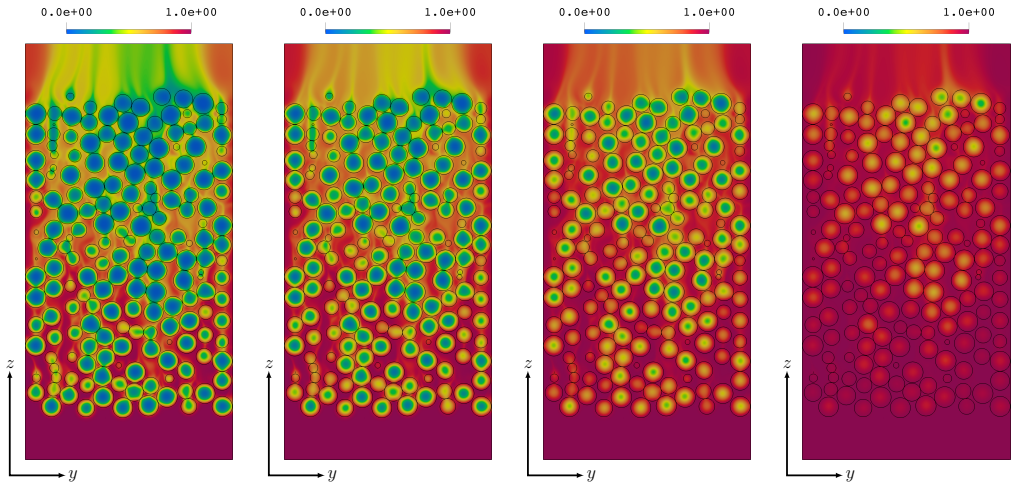

(a) $t \approx 550s$ (b) $t \approx 840s$ (c) $t \approx 1275s$ (d) $t \approx 1920s$

Figure 16: Normalized bulk ($\frac{c_b}{c_b^{in}}$) and particle pore ($\frac{c_p}{c_b^{in}}$) phase concentrations in central y-z plane of SM column at different times. Direction of flow is upward.

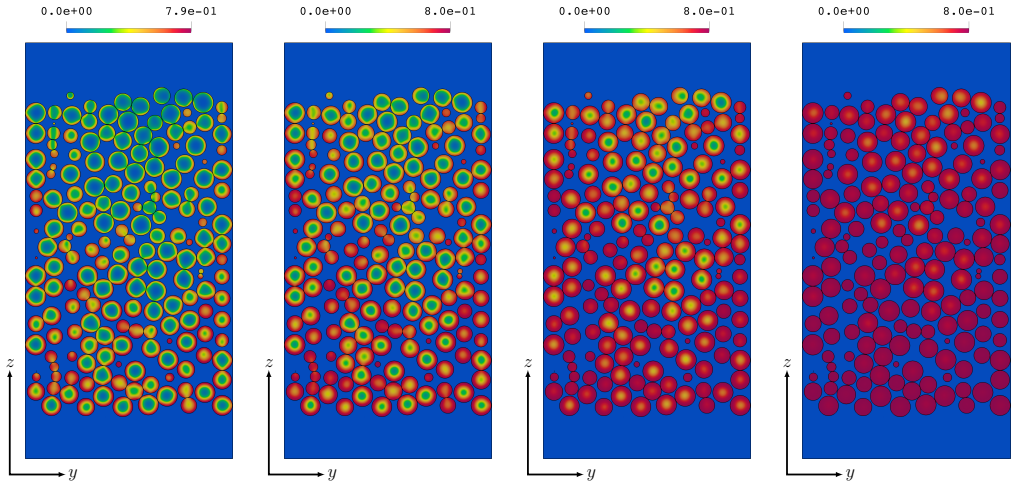

(a) $t \approx 550s$ (b) $t \approx 840s$ (c) $t \approx 1275s$ (d) $t \approx 1920s$

Figure 17: Normalized solid phase concentration ($\frac{c_s}{c_s^{max}}$) in central y-z plane of SM column at different times.

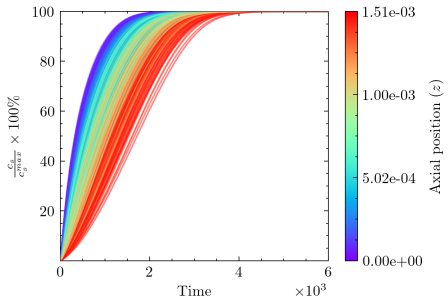

(a) SM loading curves over time

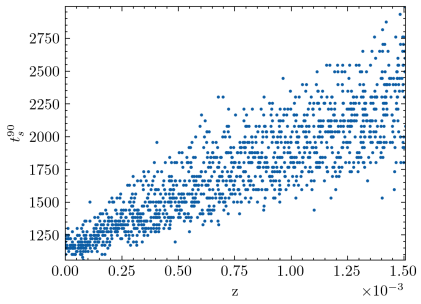

(b) SM 90% loading times over axial position

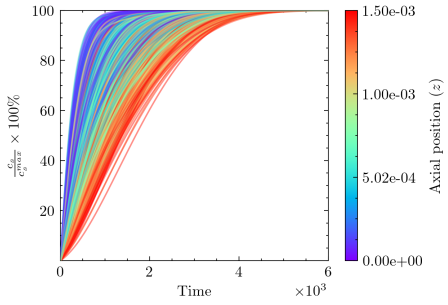

(c) SP loading curves over time

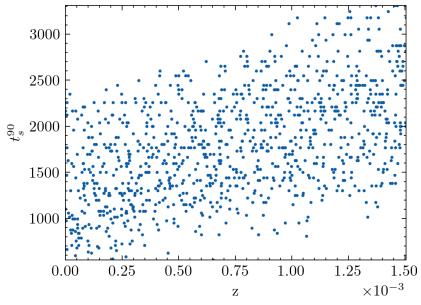

(d) SP 90% loading times over axial position

Figure 18: Effect of axial position on particle loading curves (left) and 90% loading time (right) in SM (top) and SP (bottom) simulations.

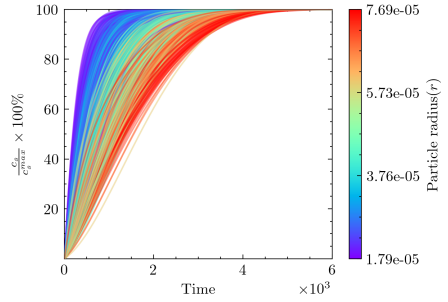

(a) Loading curves over time

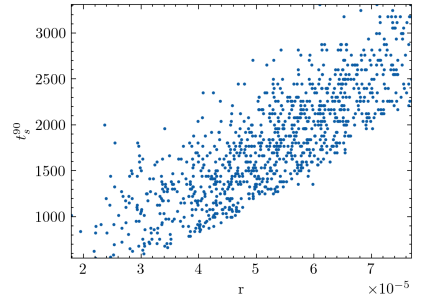

(b) 90% loading times over particle radius

Figure 19: Effect of particle radius on particle loading curves (left) and 90% loading time (right) SP simulations.

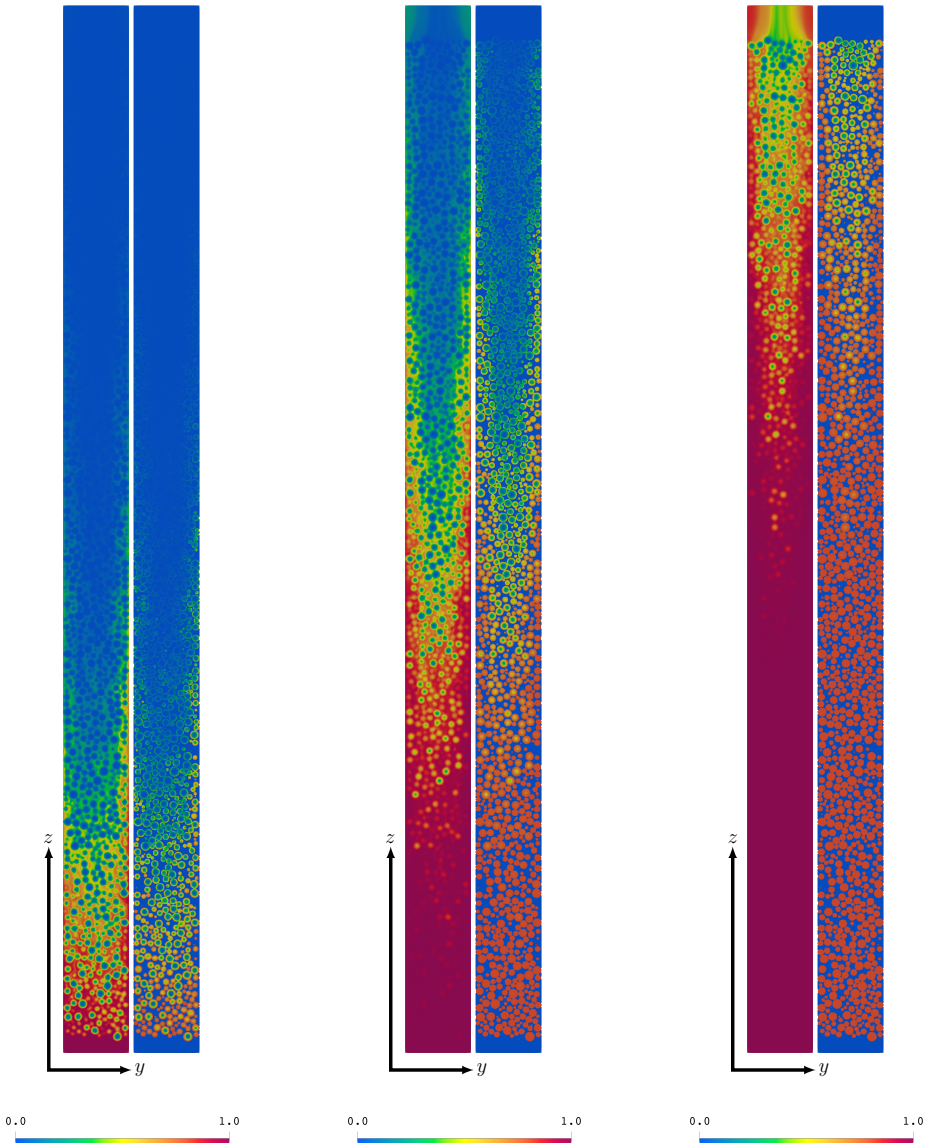

(a) $t = 1500s$ (b) $t = 4500s$ (c) $t = 7500s$

Figure 20: Central y-z plane of normalized bulk ($\frac{c_b}{c_b^{in}}$), particle pore ($\frac{c_p}{c_b^{in}}$) and solid ($\frac{c_s}{c_s^{max}}$) phase concentrations in LP simulation at different times. Direction of flow is upward.

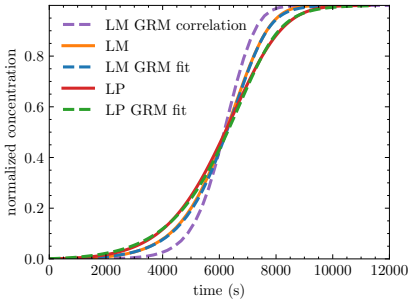

Figure 21: Breakthrough curves of LM and LP columns as simulated using the HD model and the GRM with fitted dispersion coefficient, and of LM column as simulated using the GRM with dispersion coefficient from empirical correlation.

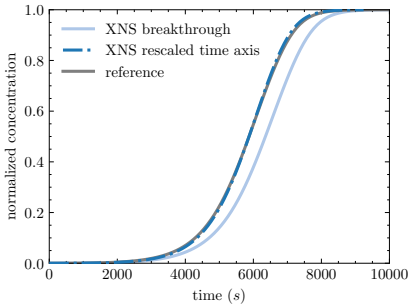

Figure 22: GRM based evaluation of BTC rescaling by holdup volume ratio $\varrho = 1.082$.

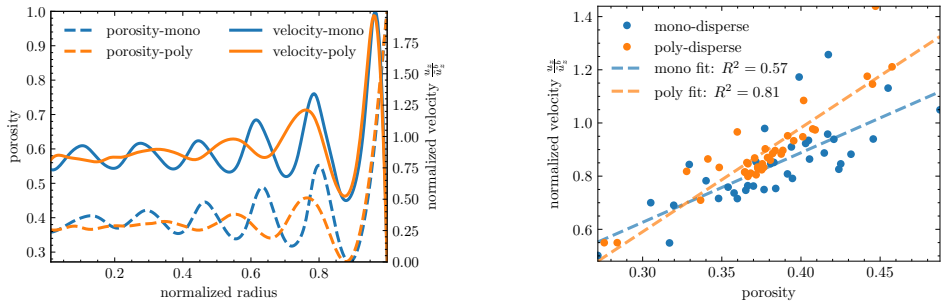

(a) Porosity and normalized velocity over column radius

(b) Linear regression of normalized velocity over porosity

Figure 23: Porosity and normalized velocity profiles and their correlations for LM and LP columns.